buildings

MDPI

Article

Equivalent SDOF Models for Estimating Isolation-Layer Energy Dissipation in Base-Isolated Tall Buildings under Strong Winds

Xiaoxin Qian [1,*], Daiki Sato [2] and Dave Montellano Osabel [2]

[1] School of Environment and Society, Tokyo Institute of Technology, Yokohama 226-8503, Japan
[2] Institute of Innovative Research, Tokyo Institute of Technology, Yokohama 226-8503, Japan; sato.d.aa@m.titech.ac.jp (D.S.); osabel.d.aa@m.titech.ac.jp (D.M.O.)
* Correspondence: qian.x.aa@m.titech.ac.jp

Abstract: An isolation layer composed of isolators and steel dampers in base-isolated tall buildings can dissipate wind-induced energy via repeated elasto-plastic deformation. Its energy dissipation can be used to estimate its wind-induced responses and the fatigue damage in the steel dampers. Computationally costly time history analyses using multi-degree-of-freedom (MDOF) models suggest that some structural parameters influence the isolation-layer energy dissipation. However, using common single-degree-of-freedom (CS) models cannot fully capture such influences (e.g., those caused by the damping ratio and the natural period of the upper structure). Hence, this paper proposes a more accurate new equivalent single-degree-of-freedom (ES) model to estimate the isolation-layer energy dissipation in base-isolated tall buildings under strong winds. The ES model considers the influence of structural parameters and uses the first mode shapes of the MDOF models. It is as computationally efficient as, but is more accurate than, the CS model. The results indicate that it can estimate the isolation-layer energy dissipation as closely as MDOF models of base-isolated tall-building under strong winds.

Keywords: base-isolated building; base isolation layer; steel damper; wind force; energy dissipation; equivalent model

Citation: Qian, X.; Sato, D.; Osabel, D.M. Equivalent SDOF Models for Estimating Isolation-Layer Energy Dissipation in Base-Isolated Tall Buildings under Strong Winds. *Buildings* **2024**, *14*, 329. https://doi.org/10.3390/buildings14020329

Academic Editor: Shaohong Cheng

Received: 26 December 2023
Revised: 17 January 2024
Accepted: 22 January 2024
Published: 24 January 2024

1. Introduction

Recently, base isolation systems have been applied to many tall buildings to ensure their structural safety during earthquakes [1–3]. They are mainly composed of (i) isolators such as rubber bearings and (ii) dampers such as viscous, viscoelastic, and steel dampers [4]. Steel dampers are most commonly used in base isolation systems due to their low cost and high performance [5,6]. For example, they require little maintenance and can dissipate seismic energy via repeated elasto-plastic deformation to minimize structural damage. In the seismic design of base-isolated tall buildings, structural designers can decrease the yield shear force coefficient of the steel dampers to promote the building's seismic performance because these dampers yield early, so they can dissipate a great amount of seismic energy after yielding.

In earthquake- and typhoon-prone areas such as Japan, the wind-resistant performance of base-isolated tall buildings should also be addressed [7–10]. However, for those base-isolated tall buildings equipped with steel dampers, promoting their seismic performance by, for example, decreasing the yield shear force coefficient of the steel dampers means demoting their wind-resistant performance. This is because these dampers may result in significant elasto-plastic responses in the base isolation layer, as they yield easily during strong winds. For example, the maximum deformation of the base isolation layer can reach around 10 cm in typhoon simulations [11]. Moreover, a study has shown that isolators with nonlinear damping perform better at a high frequency than with linear damping [12]. Another more important aspect is that wind forces have a much longer duration than

seismic forces, which may lead to the accumulation of fatigue damage in yielding dampers. For example, the typhoon simulation results show that the fatigue damage in steel dampers can even be close to 1.0 in certain typhoon samples [13]. Suppose those fatigue-damaged dampers are not replaced in time: fatigue fracture may occur in those dampers during the next large earthquake [14,15], eventually leading to a decrease in the seismic performance of the building. However, only a few studies have been conducted on the wind-induced responses of base isolation layers, as well as the fatigue damage in steel dampers, because the current wind-resistant design in Japan is based on buildings behaving elastically under strong winds [16].

An energy balance method has been established by balancing the seismic energy input and isolation layer energy dissipation, suggesting that the seismic responses of the base isolation layer can be estimated as long as the isolation layer energy dissipation is obtained [17]. Similarly, the wind-induced responses of the base isolation layer can also be estimated if the isolation layer energy dissipation is obtained [18–23]. On the other hand, the isolation layer energy dissipation will be very close to the steel damper energy dissipation when the duration of the wind forces is long enough [23]. In relevant fields, D. Rigon et al. estimated the multiaxial fatigue behavior of C45 steel specimens by using the energy dissipation [24]. From the above study, we can infer that damper fatigue damage is highly relevant to the isolation layer energy dissipation. Hence, studying the isolation layer energy dissipation can help estimate the wind-induced responses of the base isolation layer and fatigue damage in the steel dampers.

Multi-degree-of-freedom (MDOF) models with multi-story wind forces are commonly analyzed in time history analyses to effectively estimate the isolation layer energy dissipation in base-isolated tall buildings under strong winds. However, time history analysis is time-consuming because MDOF models have many parameters [11,13], and multi-story wind forces should consider ensemble methods [25,26]. Hence, for efficient time history analysis, proposing a single-degree-of-freedom (SDOF) model with only a one-story force that can also be used to estimate the isolation layer energy dissipation is required. Such efficiency is highly desired, especially when assessing the resiliency of a structure after a major event [27,28]. In previous studies, two types of SDOF models have been proposed in earthquake engineering. One is a common single-degree-of-freedom (CS) model assuming the upper structure is a rigid body (Appendix A). The CS model does not consider the upper structure's characteristics (natural period and damping ratio), and all its structural parameters are calculated based on the assumption of a rigid upper structure. The other is a single-degree-of-freedom model proposed by Kasai et al. [29]. It considers the upper structure characteristics, but the calculation of its partial structural parameters (mass and wind force) is also based on the assumption of a rigid upper structure rather than a soft upper structure, the same as in the CS model. Obviously, the above two SDOF models are not appropriate for base-isolated tall buildings in wind engineering, and there is no appropriate SDOF model at present.

In view of the above, this paper aims to propose a new equivalent single-degree-of-freedom (ES) model to estimate the isolation layer energy dissipation in base-isolated tall buildings under strong winds. The ES model must meet both of the following requirements: (i) the upper structure characteristics are considered and (ii) the calculation of all the structural parameters is based on a soft upper structure. Structural engineers need this ES model to decrease the computing time for efficient wind-resistant design like the CS model and to accurately estimate the isolation-layer energy dissipation like the MDOF model. This paper first investigated the influences of the structural parameters on the isolation-layer energy dissipation in MDOF models using time history analyses (Section 2). Next, considering these influences, a modeling method for the ES model based on the first mode of the MDOF model was described (Section 3). Then, the accuracy of the isolation-layer energy dissipation in the ES model was verified by comparing the isolation-layer energy dissipation in the ES model and MDOF model (Section 4). Finally, conclusions and related remarks are given (Section 5).

2. Isolation-Layer Energy Dissipation in MDOF Models

The base-isolated tall building considered in this paper (Figure 1a) was idealized into a theoretical shear-type MDOF model (Figure 1b). Its upper structure, with assumed dimensions of height $H_u = 100$ m (u denotes upper structure), width $B_u = 25$ m, and depth $D_u = 25$ m, is expressed using an elastic 10-degree-of-freedom model (herein viewed as a 10-story model). Its isolation layer, composed of rubber bearings and steel dampers, is expressed using an elasto-plastic SDOF model. More details about the MDOF model are provided in Sections 2.1–2.4.

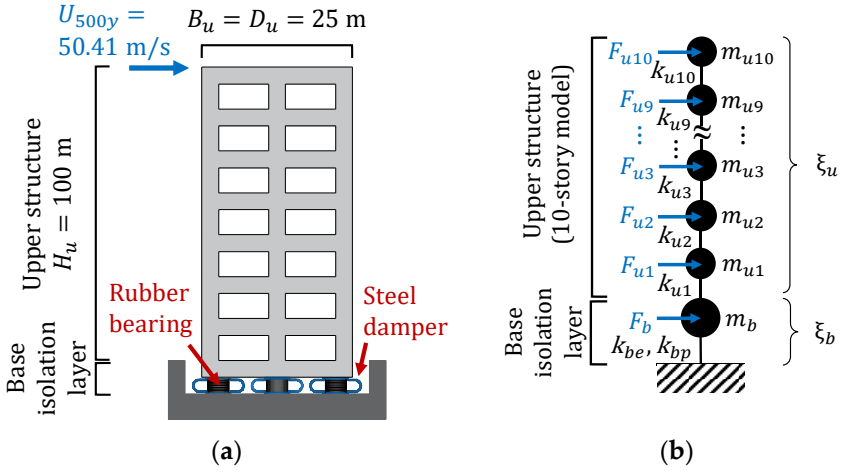

Figure 1. (**a**) Base-isolated tall building and (**b**) its idealized shear-type MDOF model.

2.1. Wind Forces of MDOF Models

The 500-year return period wind speed at the top of the building $U_{500y} = 50.41$ m/s in Figure 1a was obtained based on a basic wind speed of 36 m/s and surface roughness category III [30]. The wind force at the i-th story of the upper structure F_{ui} ($i = 1, 2, \ldots, 10$) in Figure 1b was calculated for a 700-s duration at a 0.05-s time interval, using U_{500y} and the story wind force coefficient obtained from the wind tunnel test [30]. Note that the wind force at the isolation layer $F_b = 0$ (b denotes the base isolation layer).

A total of 40 cases of wind forces (herein referred to as Force 01~40) in the along-wind and across-wind directions are considered in this paper [25,26]. As an example, Figure 2 shows the wind forces at the 10th story of the upper structure F_{u10} (Force 01), in which the along-wind direction has a mean component while the across-wind direction has none. Note that the first and last 50-s wind forces are envelopes used to avoid transient responses of the MDOF models in the time history analysis. Therefore, they are not considered in the calculation of the isolation-layer energy dissipation, as will be presented in Section 2.4.

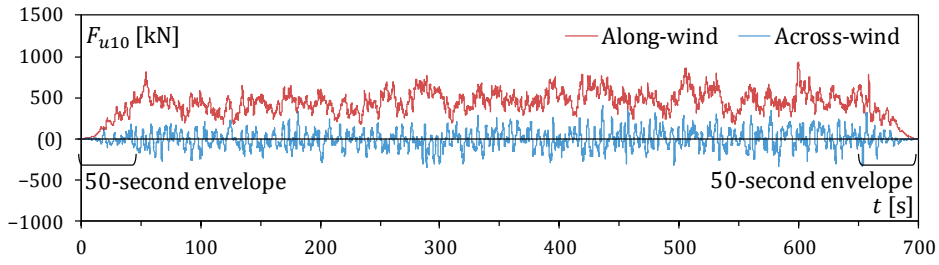

Figure 2. Wind forces at the 10th story of the upper structure F_{u10} (Force 01).

2.2. Modeling Method for the MDOF Models

For the MDOF model in Figure 1b, the mass of the i-th story of the upper structure m_{ui} is expressed as:

$$m_{ui} = \frac{\rho_u \cdot H_u \cdot B_u \cdot D_u}{10} (i = 1, 2, \ldots, 10) \tag{1}$$

where ρ_u is the density of the upper structure of the base-isolated tall building (=250 kg/m^3).

Using m_{ui} as obtained from Equation (1), the stiffness of the i-th story of the upper structure k_{ui} can be expressed by [31]:

$$k_{ui} = \begin{cases} \frac{(2\pi/T_u)^2 \cdot m_{u1} \cdot \varphi_{u1} + k_{u2}(\varphi_{u2} - \varphi_{u1})}{\varphi_{u1}} & (i = 1) \\ \frac{(2\pi/T_u)^2 \cdot m_{ui} \cdot \varphi_{ui} + k_{u(i+1)}(\varphi_{u(i+1)} - \varphi_{ui})}{\varphi_{ui} - \varphi_{u(i-1)}} & (i = 2, 3, \ldots, 9) \\ \frac{(2\pi/T_u)^2 \cdot m_{u10} \cdot \varphi_{u10}}{\varphi_{u10} - \varphi_{u9}} & (i = 10) \end{cases} \tag{2}$$

where T_u is the natural period of the upper structure of the MDOF model (the values are presented in Section 2.3) and φ_{ui} is the mode shape of the i-th story in $\{\varphi_u\}$. Here, $\{\varphi_u\}$ is the first mode shape of the upper structure of the MDOF model, assumed as a straight distribution, which is commonly used in modeling.

Assuming the upper structure is a stiffness-proportional damping model, the damping coefficient of the i-th story of the upper structure c_{ui} using k_{ui} obtained from Equation (2) is given by:

$$c_{ui} = \frac{\xi_u \cdot T_u \cdot k_{ui}}{\pi} \tag{3}$$

where ξ_u is the damping ratio of the upper structure of the MDOF model (values are presented in Section 2.3).

On the other hand, the mass of the isolation layer m_b can be written as:

$$m_b = \rho_b \cdot B_u \cdot D_u \tag{4}$$

where ρ_b is the areal density of the isolation layer of the base-isolated tall building (=3644 kg/m^2).

Furthermore, the other parameters of the isolation layer can be computed using the shear force–deformation relationship of the rubber bearing (Q_f-δ_f relationship), steel damper (Q_s-δ_s relationship), and isolation layer (Q_b-δ_b relationship), as shown in Figure 3a–c. Here, f and s denote the rubber bearing and steel damper, respectively.

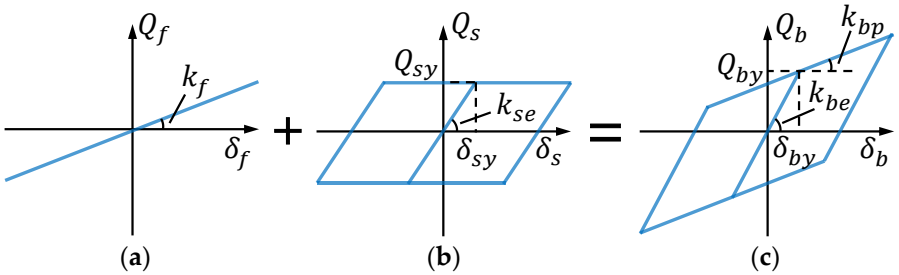

Figure 3. Shear force–deformation relationship: (**a**) rubber bearing (Q_f-δ_f relationship), (**b**) steel damper (Q_s-δ_s relationship), and (**c**) isolation layer (Q_b-δ_b relationship).

First, for the rubber bearing modeled as linearly elastic (Figure 3a), the stiffness k_f is defined as [4]:

$$k_f = \frac{4\pi^2 \left(m_b + \sum_{i=1}^{10} m_{ui} \right)}{T_f^2} \tag{5}$$

where T_f is the isolated period of the MDOF model or the natural period of the MDOF model with a rigid upper structure and no steel damper (values are presented in Section 2.3).

Next, for the steel damper modeled using an elastic–perfectly plastic model (Figure 3b), the yield shear force Q_{sy} (y denotes the yield) and initial stiffness k_{se} (e denotes the elastic range) are described as follows [4]:

$$Q_{sy} = \left(m_b + \sum_{i=1}^{10} m_{ui} \right) g \cdot \alpha_{sy} \tag{6}$$

$$k_{se} = \frac{Q_{sy}}{\delta_{sy}} \tag{7}$$

where g is the gravitational acceleration, α_{sy} is the yield shear force coefficient of the steel damper in the MDOF model (values are presented in Section 2.3), and δ_{sy} is the yield deformation of the steel damper in the MDOF model (values are presented in Section 2.3).

Finally, for the isolation layer with bilinear behavior (Figure 3c) due to combining the rubber bearing (Figure 3a) and steel damper (Figure 3b), the initial stiffness k_{be}, post-yield stiffness k_{bp} (p denotes plastic range), yield deformation δ_{by}, and yield strength Q_{by} can be formulated, respectively, as follows [4]:

$$k_{be} = k_f + k_{se} \tag{8}$$

$$k_{bp} = k_f \tag{9}$$

$$\delta_{by} = \delta_{sy} \tag{10}$$

$$Q_{by} = \delta_{by} \cdot k_{be} \tag{11}$$

Note that for the isolation layer, the damping coefficient $c_b = 0$ because the damping ratio is assumed to be $\xi_b = 0$.

2.3. Structural Parameters and Their Influences on MDOF Models

According to the equations in Section 2.2, certain structural parameters determine the behavior of the MDOF model and therefore may subsequently influence the isolation-layer energy dissipation. These structural parameters and their values [32] are as follows:

(a) Damping ratio of the upper structure

$$\xi_u = 1\%,\ 2\%,\ \text{and}\ 5\%.$$

(b) Natural period of the upper structure

$$T_u = 1.5\ \text{s},\ 2.0\ \text{s},\ 2.5\ \text{s},\ 3.0\ \text{s},\ \text{and}\ 3.5\ \text{s}.$$

(c) Isolated period

$$T_f = 4.0\ \text{s},\ 4.5\ \text{s},\ 5.0\ \text{s},\ 5.5\ \text{s},\ \text{and}\ 6.0\ \text{s}.$$

(d) Yield shear force coefficient of the steel damper

$$\alpha_{sy} = 0.020,\ 0.025,\ 0.030,\ 0.035,\ \text{and}\ 0.040.$$

(e) Yield deformation of the steel damper

$$\delta_{sy} = 1.5\ \text{cm},\ 2.0\ \text{cm},\ 2.5\ \text{cm},\ 3.0\ \text{cm},\ \text{and}\ 3.5\ \text{cm}$$

The influences of these structural parameters on the MDOF model obtained from Section 2.2 are investigated in this section, and the findings are used for detailed discussions on the isolation-layer energy dissipation in Section 2.4.

Figure 4a shows the mass distribution for the upper structure obtained from Equation (1). The masses of all stories have the same value, and they are not influenced by the above five structural parameters. Figure 4b shows the stiffness distribution for the upper structure obtained from Equation (2). The stiffness decreases with the story level for each value of T_u, and the upper structure with a long T_u shows a low stiffness. Among the five structural parameters, only T_u has an influence on the stiffness distribution. Figure 4c shows the damping coefficient distribution for the upper structure obtained from Equation (3). For $T_u = 3.0$ s, the damping coefficient for the upper structure increases with an increasing ξ_u. The same can be said for the other values of T_u. Moreover, by comparing the damping coefficient for $T_u = 3.0$ s and 3.5 s, the upper structure with a longer T_u shows a lower damping coefficient. Overall, only ξ_u and T_u can influence the damping coefficient for the upper structure.

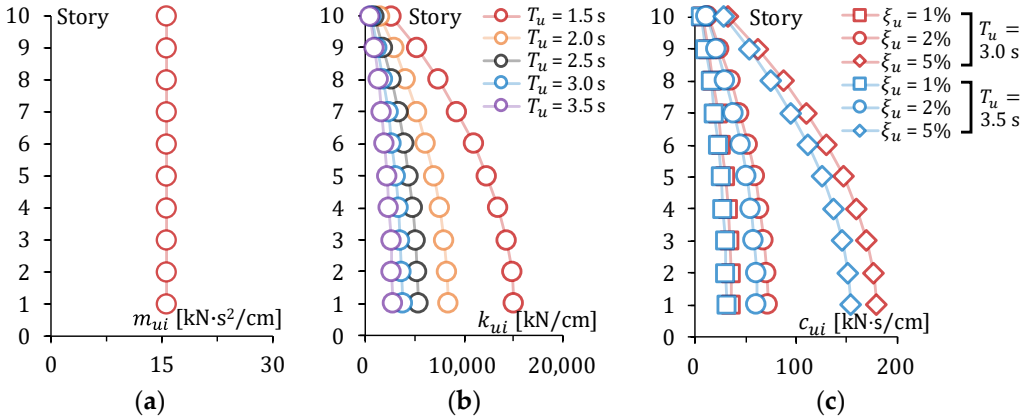

Figure 4. (**a**) Mass, (**b**) stiffness, and (**c**) damping coefficient distribution for the upper structure.

Figure 5a–d show the influences of the different structural parameters (T_u, T_f, α_{sy}, and δ_{sy}) on the shear force–deformation relationship of the isolation layer (Q_b-δ_b relationship) obtained from Equations (8)–(11). As indicated in Figure 5a, T_u does not influence the Q_b-δ_b relationship since it is not used for calculating any parameter of the isolation layer. The same can be said for the influence of ξ_u. As indicated in Figure 5b, T_f has a small influence on both the elastic and plastic ranges. As T_f increases, the initial stiffness decreases, leading to a decreasing yield shear force, and the post-yield stiffness also decreases. This is because the increase in T_f results in a decrease in k_f (Equation (5)), which then results in a decreasing k_{be} (Equation (8)) and k_{bp} (Equation (9)). As indicated in Figure 5c, α_{sy} has a significant influence on the elastic range but none on the plastic range. As α_{sy} increases, the initial stiffness increases, leading to an increasing yield shear force, while the post-yield stiffness remains unchanged. This is due to the fact that an increasing k_{se} with an increasing α_{sy} (Equations (6) and (7)) can lead to an increase in k_{be} (Equation (8)). As indicated in Figure 5d, δ_{sy} also has a significant influence on the elastic range but none on the plastic range. As δ_{sy} increases, the initial stiffness decreases, leading to a large yield shear force and yield deformation. The reason for this may be related to Equations (7) and (8).

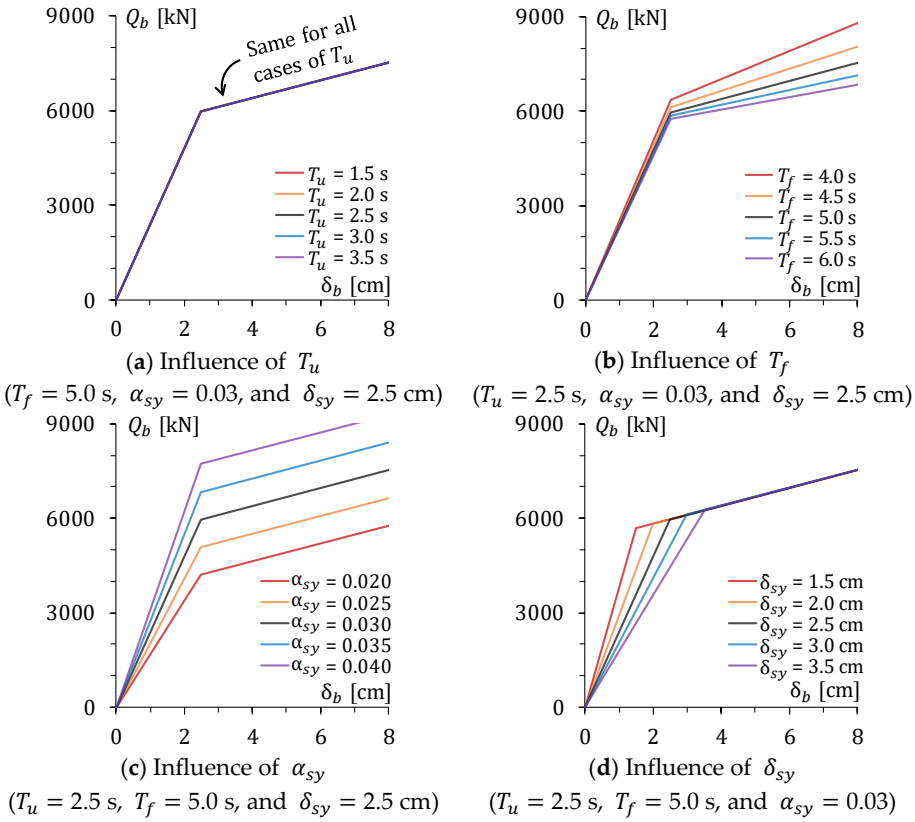

Figure 5. Shear force–deformation relationship of the isolation layer (Q_b-δ_b relationship).

2.4. Influences of the Structural Parameters on the Isolation-Layer Energy Dissipation

After performing time history analysis for the MDOF model (Section 2.2) subjected to the wind forces (Section 2.1) considering different values of the structural parameters (Section 2.3), the isolation-layer energy dissipation in the isolation layer of the MDOF model (per second [23]) $\dot{W}_b$ is obtained as follows:

$$\dot{W}_b = \frac{1}{t_1 - t_0} \int_{t_0}^{t_1} Q_b \cdot \dot{\delta}_b dt \tag{12}$$

where $\dot{\delta}_b$ is the derivative of δ_b with respect to time. As explained in Section 2.1, $t_0 = 50$ s, and $t_1 = 650$ s.

Figure 6a–d show the isolation-layer energy dissipation in the isolation layer of the MDOF model (per second) $\dot{W}_b$ obtained from Equation (12) considering the different values of the structural parameters. Note that each value of $\dot{W}_b$ is the ensemble average for Force 01~40. In the following, the $\dot{W}_b$ value in the across- and along-wind directions are discussed separately due to their different results.

In the across-wind direction, $\dot{W}_b$ increases significantly with the increase in T_u, as shown in Figure 6a. For each value of ξ_u, $\dot{W}_b$ increases by more than 6 times as T_u ranges from 1.5 s to 3.5 s. Although T_u has no influence on the Q_b-δ_b relationship (Figure 5a), it influences the stiffness distribution for the upper structure (Figure 4b). It follows that the MDOF model with a soft upper structure (a long T_u) tends to have significant wind responses, including a large deformation of the base-isolation layer that results in a great amount of $\dot{W}_b$. In Figure 6b, $\dot{W}_b$ in the across-wind direction increased slightly with the increase in T_f. For $T_f = 4 \sim 6$ s, $\dot{W}_s$ ranges from 670.2 kN·cm/s to 871.0 kN·cm/s for $\xi_u = 1\%$, from 434.5 kN·cm/s to 647.0 kN·cm/s for $\xi_u = 2\%$, and from 136.4 kN·cm/s to 298.6 kN·cm/s for $\xi_u = 5\%$. This slight trend in $\dot{W}_b$ is attributed to the slight decrease in

the initial and post-yield stiffness of the isolation layer with an increasing T_f (Figure 5b). In Figure 6c, $\dot{W}_b$ in the across-wind direction decreases significantly with the increase in α_{sy}. $\dot{W}_b$ decreases by 71.8% for $\xi_u = 1\%$, by 85.1% for $\xi_u = 2\%$, and by 96.6% for $\xi_u = 5\%$, as α_{sy} increases from 0.02 to 0.04. This significant decrease is due to the significant increase in the yield shear force of the isolation layer with an increasing T_f (Figure 5c), leading to difficulty in dissipating the wind-induced energy with the damper yielding. In Figure 6d, $\dot{W}_b$ in the across-wind direction increases slightly with the increase in δ_{sy}, which is similar to the trend observed in Figure 6b. The reason for this slight trend is that the isolation layer becomes soft in the elastic range by increasing δ_{sy} (Figure 5d) so that the isolation layer can dissipate more wind-induced energy. Moreover, $\dot{W}_b$ in the across-wind direction decreases significantly with the increase in ξ_u as the other structural parameters (T_u, T_f, α_{sy}, and δ_{sy}) remain unchanged, as shown in Figure 6a–d. This is because the upper structure with a larger ξ_u can dissipate more wind-induced energy, leading to less wind-induced energy that can be dissipated by the isolation layer. Summing up, in the across-wind direction, ξ_u, T_u, and α_{sy} show significant impacts on $\dot{W}_b$, which implies that a base-isolated tall building with a large ξ_u, a large T_u, and a small α_{sy} can easily produce a significant amount of $\dot{W}_b$. Therefore, structural designers should pay special attention to this aspect when conducting the wind-resistant design of base-isolated tall buildings. Furthermore, T_f and δ_{sy} show minor impacts on $\dot{W}_b$ in the across-wind direction.

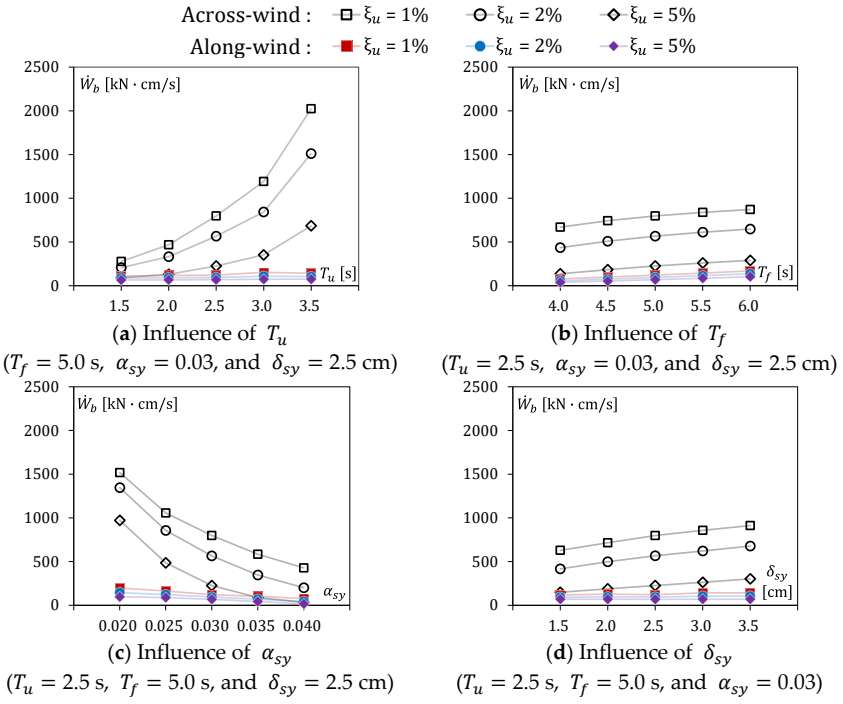

Figure 6. Isolation-layer energy dissipation of the MDOF model (per second) $\dot{W}_b$.

On the other hand, $\dot{W}_b$ in the along-wind direction is significantly small and varies negligibly with increasing structural parameters (ξ_u, T_u, T_f, α_{sy}, and δ_{sy}), as shown in Figure 6a–d. The reason for this can be explained by the Q_b-δ_b relationship for $t = 50 \sim 650$ s shown in Figure 7a,b. For a specific MDOF model ($\xi_u = 2\%$, $T_u = 2.5$ s, $T_f = 5.0$ s, $\alpha_{sy} = 0.03$, $\delta_{sy} = 2.5$ cm), the Q_b-δ_b relationship in the along-wind direction (Figure 7b) shows much fewer and smaller hysteresis loops than those in the across-wind direction (Figure 7a). This is because the wind forces in the along-wind direction have mean components (Figure 2) in the $+\delta_b$ direction, which leads to the fact that there is no large wind force in the $-\delta_b$ direction and can make the isolation layer deform plastically in the $-\delta_b$ direction.

To sum up, the above five structural parameters show negligible impacts on $\dot{W}_b$ in the along-wind direction.

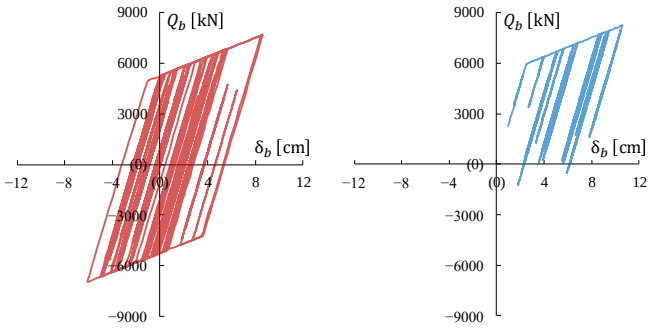

(**a**) Across-wind direction (**b**) Along-wind direction

Figure 7. Q_b-δ_b relationship ($\xi_u = 2\%$, $T_u = 2.5$ s, $T_f = 5.0$ s, $\alpha_{sy} = 0.03$, $\delta_{sy} = 2.5$ cm, Force 01, and $t = 50 \sim 650$ s).

3. Proposed Equivalent Single-Degree-of-Freedom Models

3.1. Modeling Concept

As found in Sections 2.3 and 2.4, ξ_u and T_u influence the MDOF model and therefore subsequently influence the isolation-layer energy dissipation. This contradicts the common single-degree-of-freedom (CS) model, which cannot be influenced by ξ_u and T_u (Section 1 and Table A1 in Appendix A). In order to evaluate the isolation-layer energy dissipation as accurately as the MDOF model and with the computational efficiency of the CS model (Appendix A), this paper proposes a new equivalent single-degree-of-freedom (ES) model which considers ξ_u and T_u as well as T_f, α_{sy}, and δ_{sy}.

On the other hand, for an elastic MDOF model of a tall building, its elastic first mode model can show nearly equal wind-induced responses. In addition, several structural parameters of the elastic MDOF model, including the natural period and damping ratio, can affect its elastic first mode model. Based on these findings, for the elasto-plastic MDOF model considered in this paper, its elasto-plastic first mode model (herein referred to as the ES model) is likely to show a high accuracy for the isolation-layer energy dissipation corresponding to the structural parameters of the elasto-plastic MDOF model under strong winds. For this reason, the modeling method for the ES model proposed in this paper is based on the first mode of the elasto-plastic MDOF model, as will be discussed Section 3.3. Since the MDOF model considered in this paper has elasto-plastic behavior, its first mode shape can vary with the current stiffness (initial or post-yield stiffness) of the isolation layer. As such, the possible variation in the first mode shape is investigated first in Section 3.2.

3.2. First Mode Shapes of MDOF Models

When the isolation layer deforms elastically, the eigenvalue problem of the MDOF model is expressed as:

$$\Big([K_e] - \omega_e^2[M]\Big)\{\varphi_e\} = \{0\} \tag{13}$$

where $\{\varphi_e\}$ is the elastic first mode shape of the MDOF model or the first mode shape of the MDOF model when the isolation layer deforms elastically, ω_e is the natural frequency of the MDOF model when the isolation layer deforms elastically, $[M]$ is the mass matrix of the MDOF model in which m_b and $m_{u1} \sim m_{u10}$ are used, and $[K_e]$ is the stiffness matrix of the MDOF model in which k_{be} and $k_{u1} \sim k_{u10}$ are used. The matrices $[M]$ and $[K_e]$ are given as follows:

$$[M] = \begin{bmatrix} m_b & \cdots & 0 \\ \vdots & \ddots & \vdots \\ 0 & \cdots & m_{u10} \end{bmatrix} \tag{14}$$

$$[K_e] = \begin{bmatrix} k_{be} + k_{u1} & \cdots & 0 \\ \vdots & \ddots & \vdots \\ 0 & \cdots & k_{u10} \end{bmatrix} \quad (15)$$

On the other hand, when the isolation layer deforms plastically, the eigenvalue problem of the MDOF model can be expressed by:

$$\left([K_p] - \omega_p^2 [M] \right) \{\varphi_p\} = \{0\} \quad (16)$$

where $\{\varphi_p\}$ is the plastic first mode shape of the MDOF model or the first mode shape of the MDOF model when the isolation layer deforms plastically, ω_p is the natural frequency of the MDOF model when the isolation layer deforms plastically, and $[K_p]$ is the stiffness matrix of the MDOF model in which k_{bp} and $k_{u1} \sim k_{u10}$ are used, which is given by:

$$[K_p] = \begin{bmatrix} k_{bp} + k_{u1} & \cdots & 0 \\ \vdots & \ddots & \vdots \\ 0 & \cdots & k_{u10} \end{bmatrix} \quad (17)$$

$\{\varphi_e\}$ and $\{\varphi_p\}$ as obtained from Equations (13) and (16), respectively, are then normalized to satisfy:

$$\{\varphi_e\}^T [M] \{\varphi_e\} = \{\varphi_p\}^T [M] \{\varphi_p\} = 1 \quad (18)$$

Figure 8a,b show the normalized $\{\varphi_e\}$ and $\{\varphi_p\}$ obtained from Equation (18) considering the different values of the structural parameters. Note on the vertical axis notations, b refers to the isolation layer, and Gr. refers to the ground. As indicated in Figure 8a, T_u has significant impacts on both $\{\varphi_e\}$ and $\{\varphi_p\}$ because it significantly influences the stiffness of the upper structure (Figure 2). As indicated in Figure 8b, T_f has negligible impacts on $\{\varphi_e\}$ and small impacts on $\{\varphi_p\}$ because it slightly influences the initial and post-yield stiffness of the isolation layer (Figure 5b). As indicated in Figure 8c,d, α_{sy} and δ_{sy} have small impacts on $\{\varphi_e\}$ but none on $\{\varphi_p\}$ because they have influences on the initial stiffness but none on the post-yield stiffness of the isolation layer (Figure 5c,d). These findings are used for detailed discussions of the influences of the structural parameters on ES models in Section 3.4.

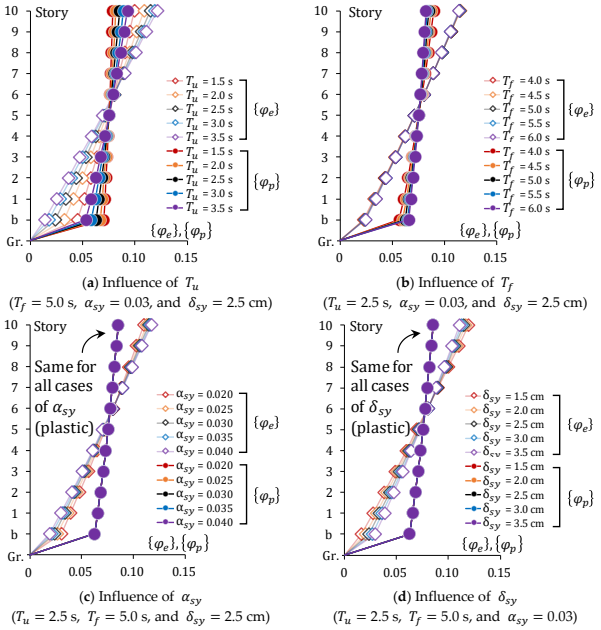

Figure 8. Normalized elastic and plastic first mode shapes, $\{\varphi_e\}$ and $\{\varphi_p\}$.

3.3. Modeling Method for ES Models

Based on the normalized $\{\varphi_e\}$ and $\{\varphi_p\}$ obtained from Section 3.2, the modeling method for the ES model is introduced in this section.

Figure 9a,b show the ES model and its shear force–deformation relationship (Q^{es}-δ^{es} relationship). According to Equation (18), the mass of the ES model m^{es} in Figure 9a can be written as:

$$m^{es} = \{\varphi_e\}^T[M]\{\varphi_e\} = \{\varphi_p\}^T[M]\{\varphi_p\} = 1 \tag{19}$$

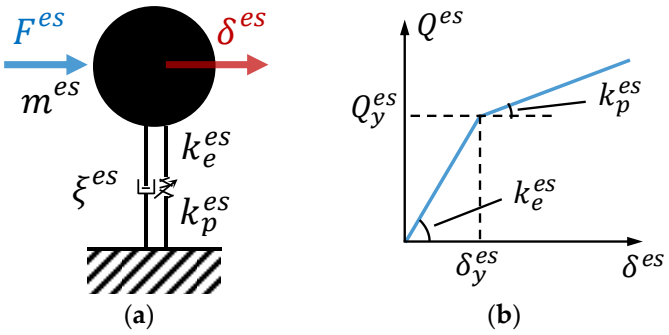

Figure 9. (**a**) ES model and (**b**) its shear force–deformation relationship (Q^{es}-δ^{es} relationship).

This indicates the mass of the ES model can be simplified into 1, while the mass of the CS model is the sum of the upper structure and base isolation-layer masses (Equations (1), (4), and (A1) in Appendix A).

Using the normalized $\{\varphi_e\}$ and $\{\varphi_p\}$, the initial and post-yield stiffness of the ES model, k_e^{es} and k_p^{es} (Figure 9b), are defined as follows:

$$k_e^{es} = \{\varphi_e\}^T[K_e]\{\varphi_e\} \tag{20}$$

$$k_p^{es} = \{\varphi_p\}^T[K_p]\{\varphi_p\} \tag{21}$$

Based on the normalized $\{\varphi_e\}$ (the reason is presented in Appendix B), the yield shear force of the ES model Q_y^{es} is described as:

$$Q_y^{es} = \{\Delta\varphi_{eb}, \Delta\varphi_{eu1}, \cdots, \Delta\varphi_{eu10}\}\begin{Bmatrix} Q_{by} \\ \varphi_{eu1(by)} \\ \vdots \\ \varphi_{eu10(by)} \end{Bmatrix} \tag{22}$$

Here, $\Delta\varphi_{eb}$, $\Delta\varphi_{eui}$, and $\varphi_{eui(by)}$ are given by:

$$\Delta\varphi_{eb} = \varphi_{eb} \tag{23}$$

$$\Delta\varphi_{eui} = \begin{cases} \varphi_{eu1} - \varphi_{eb} & (i = 1) \\ \varphi_{eui} - \varphi_{eu(i-1)} & (i = 2, 3, \ldots, 10) \end{cases} \tag{24}$$

$$\varphi_{eui(by)} = Q_{by} \cdot \frac{\Delta\varphi_{eui}}{\Delta\varphi_{eb}} (i = 1, 2, \ldots, 10) \tag{25}$$

where φ_{eb} and φ_{eui} are the mode shapes of the isolation layer and the i-th story of the upper structure in normalized $\{\varphi_e\}$.

Using Q_y^{es} and k_e^{es} as obtained from Equations (20) and (22), respectively, the yield deformation of the ES model δ_y^{es} can be written as:

$$\delta_y^{es} = \frac{Q_y^{es}}{k_e^{es}} \tag{26}$$

As indicated in Equations (20)–(22) and (26), the shear force–deformation relationship of the ES model was obtained based on $\{\varphi_e\}$ or $\{\varphi_p\}$, which is influenced by the natural period of the upper structure (Equations (2), (15), and (17)). Whereas, the natural period of the upper structure does not influence the shear force–deformation relationship of the CS model (Equations (A2)–(A5) in Appendix A).

Note that the ES model is assumed to be an initial stiffness-proportional damping model. Hence, based on the Biggs method, the damping ratio of the ES model ξ^{es} (Figure 9a) is expressed as [33]:

$$\xi^{es} = \frac{\xi_b \cdot W_b + \sum_{i=1}^{10} \xi_u \cdot W_{ui}}{W_b + \sum_{i=1}^{10} W_{ui}} \tag{27}$$

where W_b and W_{ui} are the maximum potential energy of the isolation layer and the i-th story of the upper structure, which are given based on normalized $\{\varphi_p\}$ (the reason is presented in Appendix C) as follows [33]:

$$W_b = \frac{1}{2} \cdot k_{bp} \cdot \varphi_{pb}^2 \tag{28}$$

$$W_{ui} = \frac{1}{2} \cdot k_{ui} \cdot \varphi_{pui}^2 \tag{29}$$

Here, φ_{pb} and φ_{pui} are the mode shapes of the isolation layer and i-th story of the upper structure in normalized $\{\varphi_p\}$.

As Equation (27) indicates, the damping ratio of the ES model is relevant to that of the upper structure. This is in contrast to Equation (A6) in Appendix A, where the damping ratio of the CS model is not related to the upper structure.

Based on normalized $\{\varphi_e\}$ (the reason is presented in Appendix D), the wind force of the ES model F^{es} is expressed as:

$$F^{es} = \{\varphi_e\}^T \{F\} \tag{30}$$

where $\{F\}$ is the wind force vector composed of F_b and $F_{u1} \sim F_{u10}$. This shows the wind force of the ES model is computed using the elastic first model, which is influenced by the four structural parameters (T_u, T_f, α_{sy}, and δ_{sy}) according to Equations (2), (5)–(8), and (15). Meanwhile, the wind force of the CS model is the sum of the wind forces of the upper structure and isolation layer and is irrelevant to these four structural parameters (Equation (A7) in Appendix A).

3.4. Influences of the Structural Parameters on ES Models

The influences of the structural parameters on the ES model obtained from Section 3.3 are investigated in this section, and the findings are used for detailed discussions on the accuracy verification for the isolation-layer energy dissipation in Section 4.

Figure 10a–d show the shear force–deformation of the ES model (Q^{es}-δ^{es} relationship) obtained from Equations (20)–(22) and (26) considering the different values of the structural parameters. As indicated in Figure 10a, T_u influences both the elastic and plastic ranges because it influences $\{\varphi_e\}$ and $\{\varphi_p\}$ (Figure 8a), in contrast to its lack of influence on the Q_b-δ_b relationship (Figure 5a). Note that the Q_b-δ_b relationship is in accordance with the shear force–deformation relationship of the CS model (Equations (A2)–(A5) in Appendix A). As indicated in Figure 10b, T_f has a negligible influence on the elastic range and a small influence on the plastic range due to its negligible impacts on $\{\varphi_e\}$ and small impacts on $\{\varphi_p\}$ (Figure 8b), respectively, which is similar to the Q_b-δ_b relationship (Figure 5b). As indicated in Figure 10c,d, α_{sy} and δ_{sy} have small influences on the elastic range, which is different from the Q_b-δ_b relationship (Figure 5c,d), but none on the plastic range, which is similar to the Q_b-δ_b relationship (Figure 5c,d). This is because they have small impacts on $\{\varphi_e\}$ and but none on $\{\varphi_p\}$.

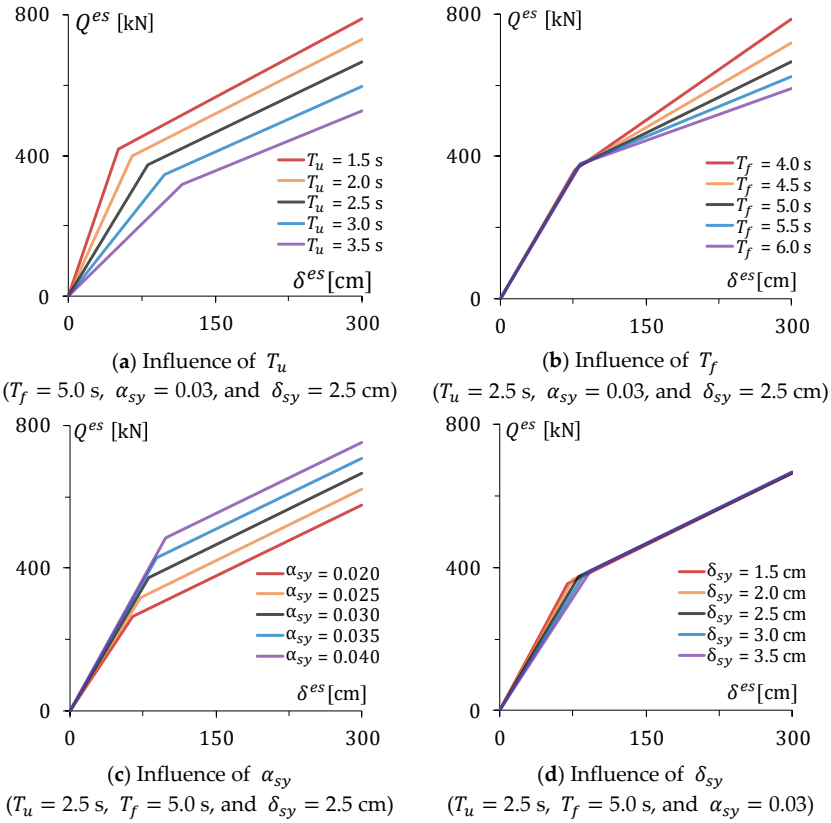

(**a**) Influence of T_u (T_f = 5.0 s, α_{sy} = 0.03, and δ_{sy} = 2.5 cm)

(**b**) Influence of T_f (T_u = 2.5 s, α_{sy} = 0.03, and δ_{sy} = 2.5 cm)

(**c**) Influence of α_{sy} (T_u = 2.5 s, T_f = 5.0 s, and δ_{sy} = 2.5 cm)

(**d**) Influence of δ_{sy} (T_u = 2.5 s, T_f = 5.0 s, and α_{sy} = 0.03)

Figure 10. Shear force–deformation of the ES model (Q^{es}-δ^{es} relationship).

Figure 11a–d show the damping ratio of the ES model ξ^{es} obtained from Equation (27) considering different values of the structural parameters. As shown in Figure 11a,b, T_u and T_f influence ξ^{es} due to their impacts on $\{\varphi_p\}$ (Figure 8a,b). In contrast, α_{sy} and δ_{sy} do not influence ξ^{es} (Figure 11c,d) because they have no impact on $\{\varphi_p\}$ (Figure 8c,d). Moreover, ξ^{es} increases with an increasing ξ_u according to Figure 11a–d.

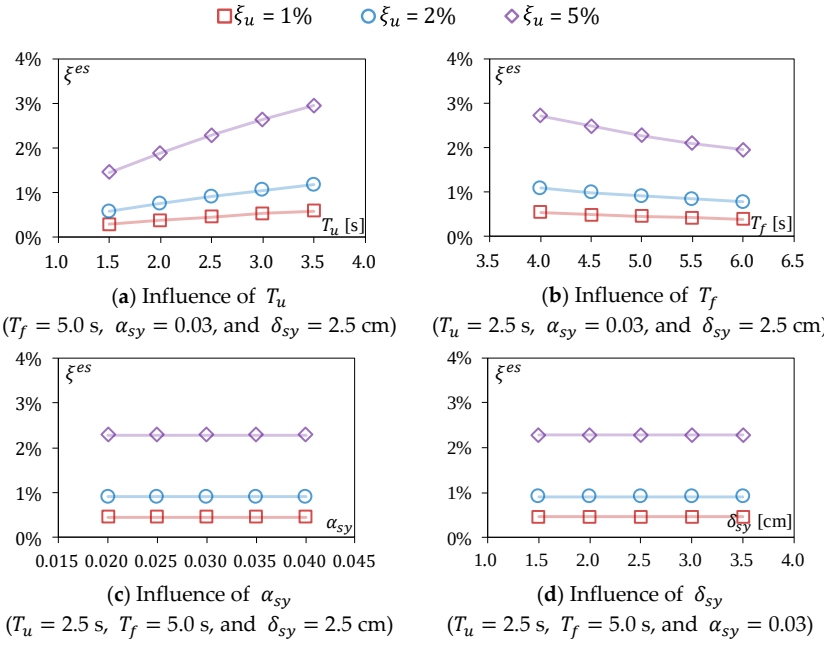

(**a**) Influence of T_u (T_f = 5.0 s, α_{sy} = 0.03, and δ_{sy} = 2.5 cm)

(**b**) Influence of T_f (T_u = 2.5 s, α_{sy} = 0.03, and δ_{sy} = 2.5 cm)

(**c**) Influence of α_{sy} (T_u = 2.5 s, T_f = 5.0 s, and δ_{sy} = 2.5 cm)

(**d**) Influence of δ_{sy} (T_u = 2.5 s, T_f = 5.0 s, and α_{sy} = 0.03)

Figure 11. Damping ratio of the ES model ξ^{es}.

Figure 12a,b show the wind forces of the ES model F^{es} considering different values of T_u ($T_f = 5.0$ s, $\alpha_{sy} = 0.03$, $\delta_{sy} = 2.5$ cm, and Force 01) obtained from Equation (30). In Figure 12a, F^{es} for $T_u = 1.5$ s nearly equals that for $T_u = 3.5$ s in the along-wind direction, which indicates T_u has a negligible influence on F^{es}. Although T_u influences $\{\varphi_e\}$, the mode shapes of the lower stories (isolation layer and 1st~5th story) and upper stories (6th~10th story) vary adversely as T_u increases (Figure 8a), which leads to the negligible influence of T_u on F^{es}. The same can be said for the influences of the other structural parameters (T_f, α_{sy}, and δ_{sy}) on F^{es}. Moreover, Figure 12b also shows the negligible influence of T_u on F^{es} in the across-wind direction for to the same reason.

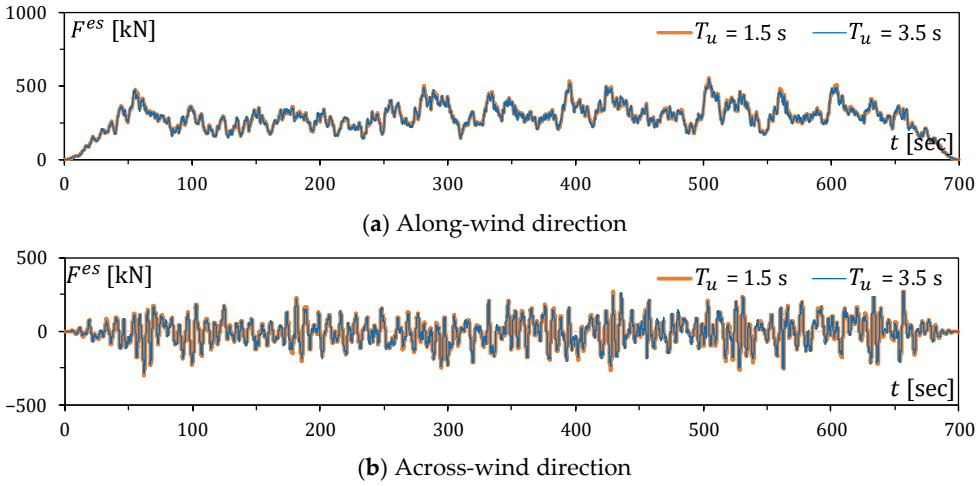

(**a**) Along-wind direction

(**b**) Across-wind direction

Figure 12. Wind forces of the ES model F^{es} considering different values of T_u ($T_f = 5.0$ s, $\alpha_{sy} = 0.03$, $\delta_{sy} = 2.5$ cm, and Force 01).

The influences of the structural parameters on the ES model are summarized in Table 1. All five structural parameters have impacts on the ES model and therefore may influence the isolation-layer energy dissipation in the ES model. This differs to Table A1 in Appendix A, where two structural parameters (ξ_u and T_u) have no impact on the CS model.

Table 1. Influences of structural parameters on the ES model.

	m^{es}	k_e^{es}	k_p^{es}	Q_y^{es}	δ_y^{es}	ξ^{es}	F^{es}
ξ_u	×	×	×	×	×	○	×
T_u	×	○	○	○	○	○	○
T_f	×	○	○	○	○	○	○
α_{sy}	×	○	×	○	○	×	○
δ_{sy}	×	○	×	○	○	×	○

○ denotes having influence and × denotes having no influence.

4. Accuracy Verification for Isolation-Layer Energy Dissipation

In order to judge whether the proposed ES model (Section 3) can be used to estimate the isolation-layer energy dissipation in base-isolated tall buildings under strong winds, this section focuses on verifying the accuracy of calculating the isolation-layer energy dissipation using the ES model by comparing the isolation-layer energy dissipation in the ES model and MDOF model in the along- and across-wind directions. In addition, the isolation-layer energy dissipation in the CS model is also verified in this section for comparison with the ES model.

After performing time history analysis for the ES model, the isolation-layer energy dissipation in the ES model (per second [23]) $\dot{W}_b^{es}$ is expressed as:

$$\dot{W}_b^{es} = \frac{1}{t_1 - t_0} \int_{t_0}^{t_1} Q^{es} \cdot \dot{\delta}^{es} dt \tag{31}$$

where Q^{es} is the shear force of the ES model, $\dot{\delta}^{cs}$ is the derivative of δ^{cs} with respect to time, and $t_0 = 50$ s and $t_1 = 650$ s (the same as Equation (12)).

Figure 13a–d show the isolation-layer energy dissipation in the ES model $\dot{W}_b^{es}$ (Equation (31)), CS model $\dot{W}_b^{cs}$ (Equation (A8) in Appendix A), and MDOF model $\dot{W}_b$ (Equation (12)) with variations in T_u and ξ_u (Figure 13a), in T_f and ξ_u (Figure 13b), in α_{sy} and ξ_u (Figure 13c), and in δ_{sy} and ξ_u (Figure 13d). The accuracy of the ES and CS models is evaluated by comparing $\dot{W}_b^{es}$ and $\dot{W}_b^{cs}$ with $\dot{W}_b$, respectively.

As indicated in Figure 13a, $\dot{W}_b^{cs}$ has constant values and a low accuracy (errors greatly exceeding 20%) in the along- and across-wind directions because T_u and ξ_u have no impact on the CS model (Table A1 in Appendix A). On the other hand, $\dot{W}_b^{es}$ shows a much higher accuracy than $\dot{W}_b^{cs}$ in the along- and across-wind directions because T_u and ξ_u influence the ES model (Table 1). Although the errors in $\dot{W}_b^{es}$ are less than 20% in the along-wind direction, these errors can be ignored because the values of $\dot{W}_b^{es}$ and $\dot{W}_b$ in the along-wind direction are significantly small. In the across-wind direction, the errors in $\dot{W}_b^{es}$ are within 20% when $\dot{W}_b < 800$ kN·cm/s and within 10% when $\dot{W}_b \geq 800$ kN·cm/s, which means $\dot{W}_b^{es}$ has a good accuracy.

As indicated in Figure 13b, $\dot{W}_b^{cs}$ also has a low accuracy (errors greatly exceeding 20%) in the along- and across-wind directions. Despite T_f influencing the CS model (Table A1 in Appendix A), the result shows it has a small impact on $\dot{W}_b^{cs}$. On the other hand, $\dot{W}_b^{es}$ also has a much higher accuracy than $\dot{W}_b^{cs}$ in the along- and across-wind directions. As explained in the preceding paragraph, the errors in $\dot{W}_b^{es}$ in the along-wind direction can be ignored.

As indicated in Figure 13c, $\dot{W}_b^{es}$ has a much higher accuracy than $\dot{W}_b^{cs}$ in the along- and across-wind directions. In the across-wind direction, the errors in $\dot{W}_b^{es}$ are approximately within 20%. However, in the large range of isolation-layer energy dissipation ($\dot{W}_b \geq 800$ kN·cm/s), the errors in $\dot{W}_b^{es}$ are within 10%.

As indicated in Figure 13d, the errors in $\dot{W}_b^{es}$ are approximately within 20% in the along- and across-wind directions. In the across-wind direction, it is observed that the error in $\dot{W}_b^{es}$ slightly decreases as $\dot{W}_b$ increases.

To sum up, the proposed ES model has a much higher accuracy of isolation-layer energy dissipation than the commonly used CS model in the along- and across-wind directions. The errors in the isolation-layer energy dissipation in the ES model are approximately less than 20%, which shows a good accuracy. Especially in the large range of isolation-layer energy dissipation ($\dot{W}_b \geq 800$ kN·cm/s in the across-wind direction), they are approximately within 10%, indicating a good accuracy. These errors are mainly due to:

(1) Partial parametric calculation of the ES model (Q_y^{es}, ζ^{es}, and F^{es}) is based on the assumption of only one mode shape ($\{\varphi_e\}$ or $\{\varphi_p\}$), as mentioned in Appendices B–D, but the isolation layer in fact shows elasto-plastic deformation under strong winds.
(2) The influence of higher-order modes may lead to these errors.

As a supplementary, Figure 14 shows an example of the time history of the accumulated isolation-layer energy dissipation in the ES model W_b^{es}, CS model W_b^{cs}, and MDOF model W_b in the across-wind direction ($\xi_u = 2\%$, $T_u = 2.5$ s, $T_f = 5.0$ s, $\alpha_{sy} = 0.03$, $\delta_{sy} = 2.5$ cm, and Force 03). W_b^{es} of the ES model is close to W_b of the MDOF model during 600 s. This demonstrates the validity of the ES model.

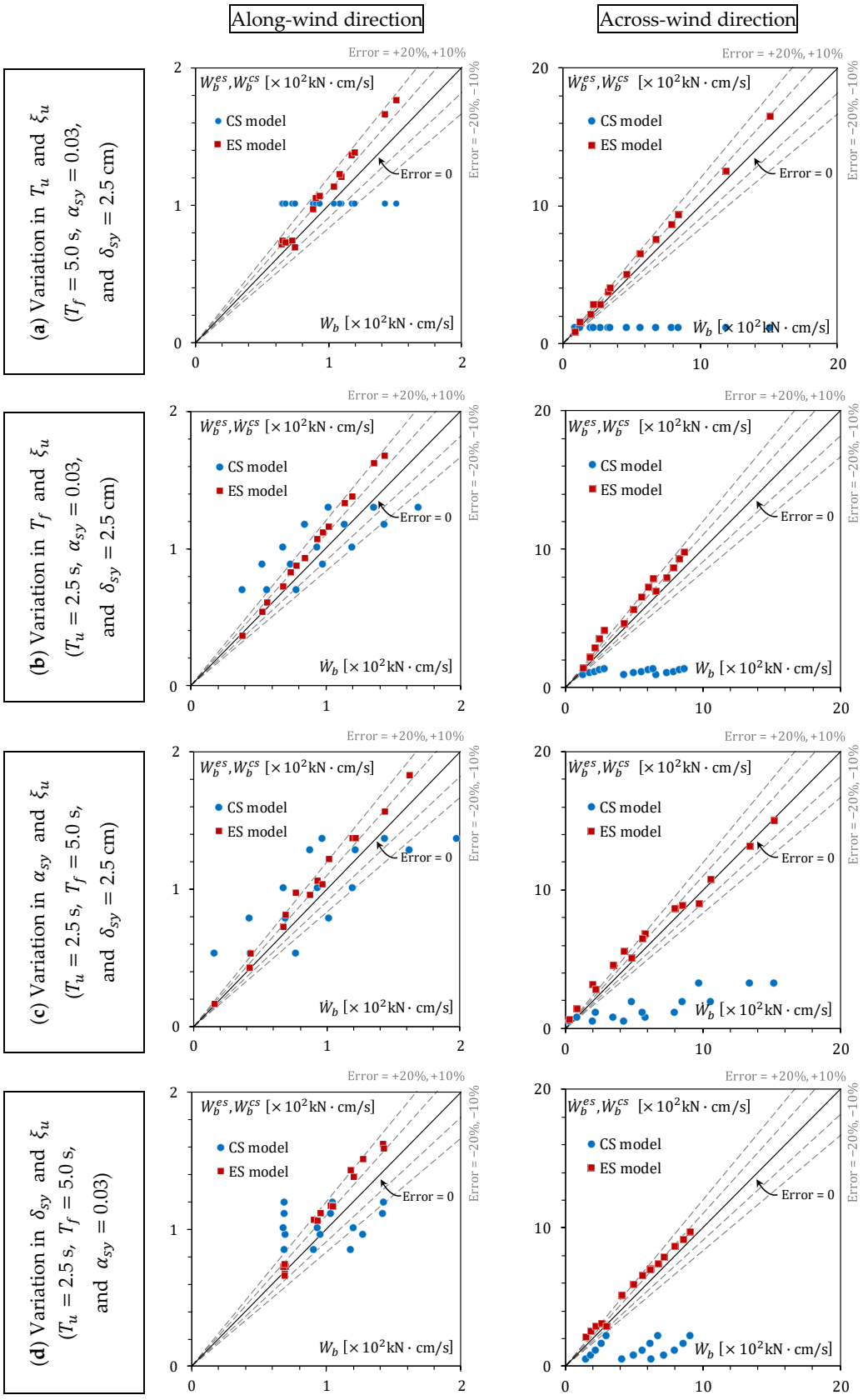

Figure 13. Isolation-layer energy dissipation in the ES model $\dot{W}_b^{es}$, CS model $\dot{W}_b^{cs}$, and MDOF model $\dot{W}_b$.

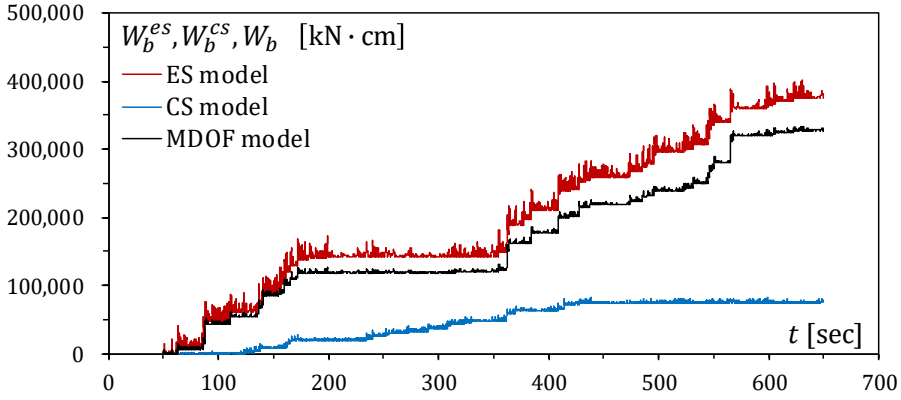

Figure 14. Time history of accumulated isolation-layer energy dissipation in the ES model W_b^{es}, CS model W_b^{cs}, and MDOF model W_b in the across-wind direction ($\xi_u = 2\%$, $T_u = 2.5$ s, $T_f = 5.0$ s, $\alpha_{sy} = 0.03$, $\delta_{sy} = 2.5$ cm, and Force 03).

5. Conclusions

This paper analyzed a theoretical shear-type multi-degree-of-freedom (MDOF) model idealized from a base-isolated tall buildings subjected to strong winds. The base isolation layer composed of rubber bearings and steel dampers was modeled as an elasto-plastic SDOF model, while the upper structure was modeled as an elastic 10-DOF model. Time history analyses revealed the influences of the five structural parameters ((i) damping ratio and (ii) natural period of the upper structure, (iii) isolated period, (iv) yield shear force coefficient, and (v) yield deformation of the steel damper) on the isolation-layer energy dissipation in the MDOF model. These findings contribute to the proposal of equivalent single-degree-of-freedom (ES) models to estimate the isolation-layer energy dissipation in base-isolated buildings under strong winds. The following conclusions are drawn from this study:

(1) In the along-wind direction, the isolation-layer energy dissipation in the MDOF model is very small and negligibly influenced by the above five structural parameters because the wind forces contain mean components.

(2) In the across-wind direction, three structural parameters (damping ratio and natural period of the upper structure and yield shear force coefficient of the steel damper) have significant impacts on the isolation-layer energy dissipation in the MDOF model, while the other two structural parameters (isolated period and yield deformation of the steel damper) have slight impacts.

(3) Considering the above findings, these five structural parameters were used in devising the ES model. Hence, their influences on the ES model are captured. This greatly contradicts the common single-degree-of-freedom (CS) model, which is not influenced by the damping ratio and natural period of the upper structure.

(4) Moreover, by considering the variation in the first mode shape of the MDOF model according to the elasto-plasticity of the base isolation layer, an appropriate first mode shape was selected for modeling the ES model. As a result, the ES model reproduces accurately the isolation-layer energy dissipation of the first mode of a base-isolated tall building against strong winds.

(5) A comparison of the isolation-layer energy dissipation in the ES and CS models versus that in the MDOF model shows the ES model outperforms the CS model.

Based on the above conclusions, structural engineers can benefit from the proposed ES model. Using the ES model, they can accurately and efficiently estimate the isolation-layer energy dissipation in base-isolated tall buildings under strong winds.

Like any other method, the ES model has its limitations as its modeling is based on the assumption of the first mode. Hence, for very tall buildings where the influence of higher-order modes is dominant, it may have significant inaccuracies. Moreover, its

modeling method is limited to base-isolated tall buildings equipped with rubber bearings (isolators) and steel dampers.

Also, directly comparing the hysteresis loops of the ES and MDOF models is impossible as the two models have different shear force–deformation relationship.

Despite the above limitations and advantages, the ES model can be used to estimate the energy dissipation in base-isolated tall buildings subjected to ground motions [34]. It can also be applied to different building configurations such as inter-story isolated tall buildings [35,36] subjected to strong winds or ground motion for time-saving analyses. Future work can address all the above limitations, e.g., extending the ES model to incorporate other types of isolators (e.g., [37]) and considering other wind effects (e.g., [38]).

Author Contributions: Conceptualization, X.Q. and D.S.; methodology, X.Q. and D.S.; software, D.S.; validation, X.Q. and D.S.; formal analysis, X.Q.; investigation, X.Q.; resources, D.S.; data curation, X.Q.; writing—original draft preparation, X.Q.; writing—review and editing, D.S. and D.M.O.; visualization, X.Q.; supervision, D.S. and D.M.O.; project administration, D.S.; funding acquisition, D.S. All authors have read and agreed to the published version of the manuscript.

Funding: This paper received funding from the JST Program on Open Innovation Platform with Enterprises, Research Institute and Academia (JPMJOP1723).

Data Availability Statement: The data presented in this study are available on request from the corresponding author. The data are not publicly available due to privacy.

Conflicts of Interest: The authors declare no conflicts of interest.

Appendix A. Modeling Method for CS Models

Figure A1a,b show the common single-degree-of-freedom (CS) model and its shear force–deformation relationship (Q^{cs}-δ^{cs} relationship). The mass m^{cs}, initial stiffness k_e^{cs}, post-yield stiffness k_p^{cs}, yield shear force Q_y^{cs}, yield displacement δ_y^{cs}, damping ratio ξ^{cs}, and wind force F^{cs} can be written, respectively, as follows:

$$m^{cs} = m_b + \sum_{i=1}^{10} m_{ui} \tag{A1}$$

$$k_e^{cs} = k_{be} \tag{A2}$$

$$k_p^{cs} = k_{bp} \tag{A3}$$

$$Q_y^{cs} = Q_{by} \tag{A4}$$

$$\delta_y^{cs} = \delta_{by} \tag{A5}$$

$$\xi^{cs} = \xi_b \tag{A6}$$

$$F^{cs} = \sum_{i=1}^{10} F_{ui} \tag{A7}$$

According to the above equations, the influences of the structural parameters on the CS model are summarized in Table A1. The three structural parameters (T_f, α_{sy}, and δ_{sy}) have impacts on the CS model and therefore may influence the isolation-layer energy dissipation in the CS model. However, the other two structural parameters (ξ_u and T_u) have no impact on the CS model, in contrast to the ES model (Table 1 in Section 3.4).

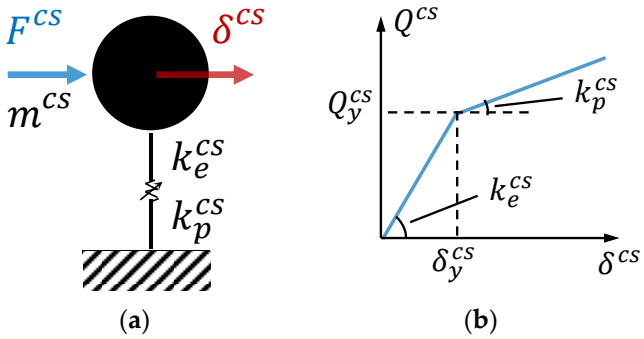

Figure A1. Equivalent stiffness of the base isolation layer k_{beq} (an example of $\mu_b = 10$).

After performing time history analyses for the CS models, the isolation-layer energy dissipation in the CS model (per second [23]) $\dot{W}_b^{cs}$ is expressed as:

$$\dot{W}_b^{cs} = \frac{1}{t_1 - t_0} \int_{t_0}^{t_1} Q^{cs} \cdot \dot{\delta}^{cs} dt \tag{A8}$$

where Q^{cs} is the shear force of the CS model and $\dot{\delta}^{cs}$ is the derivative of δ^{cs} with respect to time. Here, δ^{cs} is the deformation of the CS model. $t_0 = 50$ s and $t_1 = 650$ s (the same as Equation (12)).

Appendix B. On Selecting $\{\varphi_e\}$ for the Yield Shear Force of the ES Model Q_y^{es}

An elastic MDOF model is obtained by letting $k_{bp} = k_{be}$ of the elasto-plastic MDOF model ($\xi_u = 2\%$, $T_u = 2.5$ s, $T_f = 5.0$ s, and $\delta_{sy} = 2.5$ cm) given in Section 2. Based on the elastic MDOF model, an equivalent elastic SDOF model is then obtained using the modeling method introduced in Section 3. Note that the damping ratio of the equivalent elastic SDOF model is obtained using the Biggs method [33] based on $\{\varphi_p\}$, as will be discussed in Appendix C.

Examples of the deformation time history of the base isolation layer of the elastic MDOF model and the equivalent elastic SDOF model considering different values of α_{sy} (Force 02 in the across-wind direction and $t = 0 \sim 200$ s) are shown in Figure A2a–e. Note that the displacement of the elastic SDOF model needs to be multiplied by the mode shape of the base isolation layer in the first mode shape of the elastic MDOF model. Here, the result of the equivalent elastic SDOF model is very similar to that of the elastic MDOF model at $t = 0 \sim 200$ s, suggesting that the elastic first mode shape $\{\varphi_e\}$ is selected for the yield shear force of the ES model.

Minor discrepancies between the two results are due to (i) the minor influences of higher-order modes and (ii) the fact that only the upper structure of the elastic MDOF model follows a stiffness-proportional damping distribution, not including the base isolation layer.

Table A1. Influences of structural parameters on the CS model.

	m^{cs}	k_e^{cs}	k_p^{cs}	Q_y^{cs}	δ_y^{cs}	ξ^{cs}	F^{cs}
ξ_u	×	×	×	×	×	×	×
T_u	×	×	×	×	×	×	×
T_f	×	○	○	○	×	×	×
α_{sy}	×	○	×	○	×	×	×
δ_{sy}	×	○	×	○	○	×	×

○ denotes having influence and × denotes having no influence.

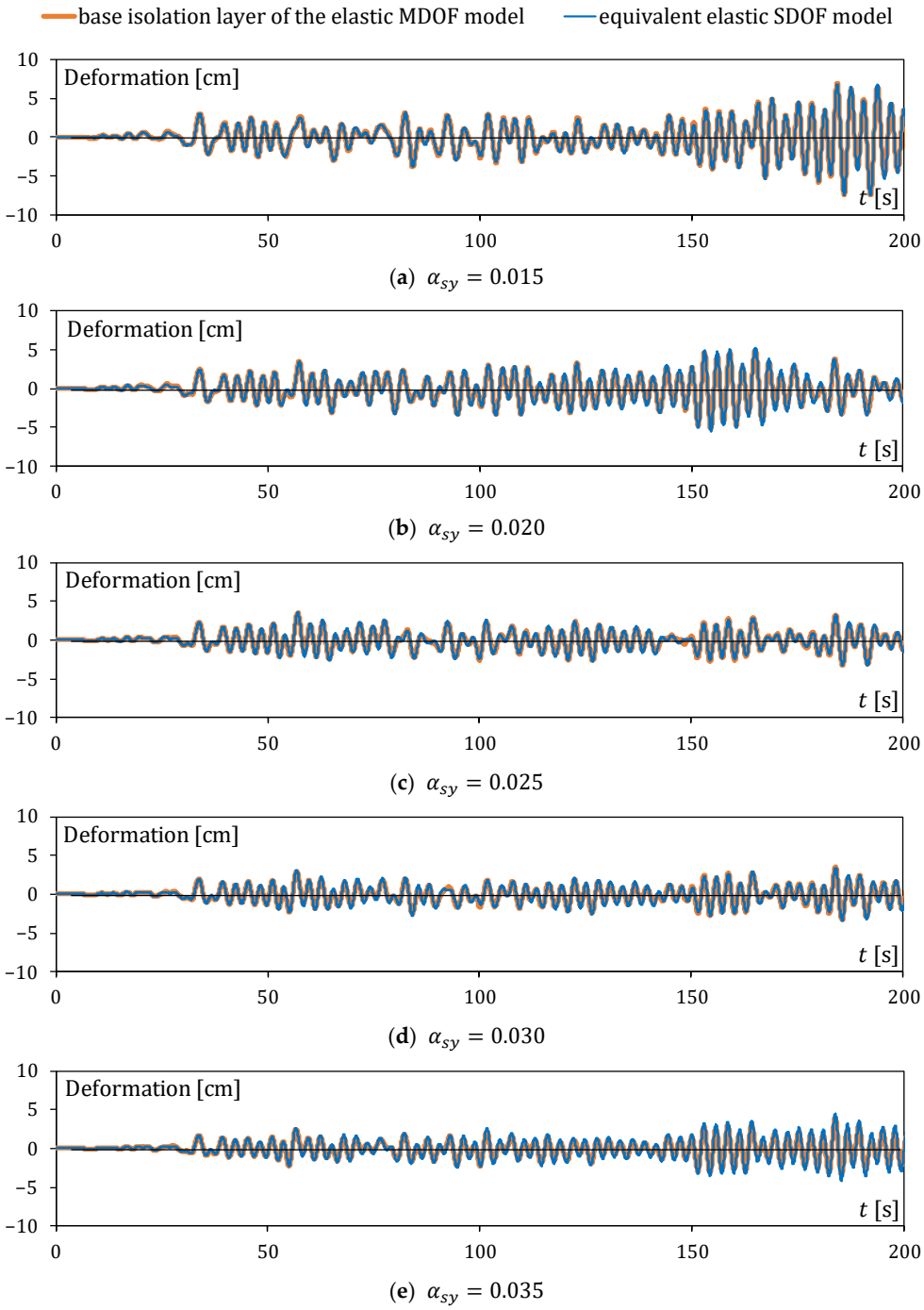

Figure A2. Deformation time history of base isolation layer of the elastic MDOF model and the equivalent elastic SDOF model (Force 02 in the across-wind direction and t = 0∼200 s).

Appendix C. On Selecting $\{\varphi_p\}$ for the Damping Ratio of the ES Model ξ^{es}

In selecting either $\{\varphi_e\}$ or $\{\varphi_p\}$ to be adopted for the damping ratio of the ES model ξ^{es}, the following are calculated and contrasted:

(i) The equivalent damping ratio of the MDOF model ξ_{eq} (obtained using the Biggs method [33]) with the equivalent stiffness of the base isolation layer k_{beq}. Here, k_{beq} is calculated based on the different ductility factors of the base isolation layer μ_b (=ratio between the maximum and yield displacements of the base isolation layer), as shown in Figure A3.

(ii) The damping ratio of the ES model ξ_e^{es} (obtained using the Biggs method [33]) considering $\{\varphi_e\}$.
(iii) The damping ratio of the ES model ξ_p^{es} (obtained using the Biggs method [33]) considering $\{\varphi_p\}$.

Figure A4 compares ξ_{eq}, ξ_e^{es}, and ξ_p^{es} ($\xi_u = 2\%$, $T_u = 2.5$ s, $T_f = 5.0$ s, $\alpha_{sy} = 0.025$, and $\delta_{sy} = 2.5$ cm). ξ_{eq} decreases as μ_b increases from 0 to 14, with ξ_e^{es} and ξ_p^{es} at the upper and lower bounds of ξ_{eq}, respectively. Desiring a conservative value for the damping ratio, ξ_p^{es} is preferred over ξ_e^{es}. Hence, the plastic first mode shape $\{\varphi_p\}$ is selected for the damping ratio of the ES model.

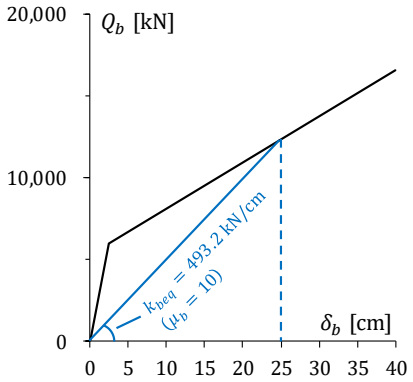

Figure A3. Equivalent stiffness of the base isolation layer k_{beq} (an example of μ_b = 10).

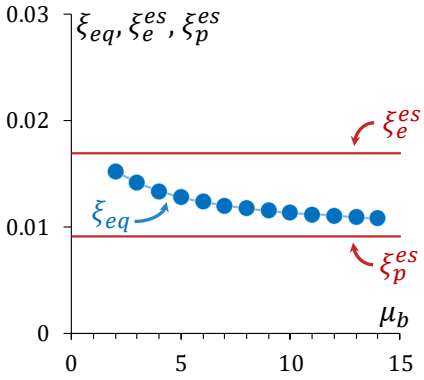

Figure A4. Comparison of ξ_{eq}, ξ_e^{es}, and ξ_p^{es} ($\xi_u = 2\%$, $T_u = 2.5$ s, $T_f = 5.0$ s, $\alpha_{sy} = 0.025$, and $\delta_{sy} = 2.5$ cm).

Appendix D. On Selecting $\{\varphi_e\}$ for the Wind Force of the ES Model F^{es}

In selecting either $\{\varphi_e\}$ or $\{\varphi_p\}$ to be adopted for the wind force of the ES model F^{es}, the following are calculated and contrasted:

(i) Standard deviation of the equivalent wind force of the MDOF model σ_{eq} (refer to Equation (30)) with k_{beq} (the same as Appendix C). Here, *eq* denotes equivalent.
(ii) Standard deviation of equivalent wind force of the ES model σ_e^{es} considering $\{\varphi_e\}$.
(iii) Standard deviation of equivalent wind force of the ES model σ_p^{es} considering $\{\varphi_p\}$.

Figure A5 compares σ_{eq}, σ_e^{es}, and σ_p^{es} ($\xi_u = 2\%$, $T_u = 2.5$ s, $T_f = 5.0$ s, $\alpha_{sy} = 0.025$, $\delta_{sy} = 2.5$ cm, and Force 02 in the across-wind direction). At a glance, there is no obvious difference between σ_{eq} (for $\mu_b = 0 \sim 14$), σ_e^{es}, and σ_p^{es}, suggesting that both $\{\varphi_e\}$ and $\{\varphi_p\}$ can be considered for calculating the wind force of the ES model. However, a closer look reveals that σ_e^{es} is a little bit higher or more conservative than σ_p^{es}. Hence, $\{\varphi_e\}$ is selected for the wind force of the ES model.

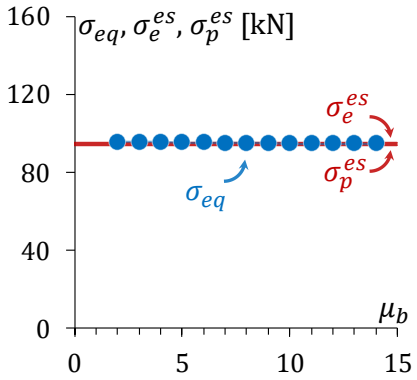

Figure A5. Comparison of σ_{eq}, σ_e^{es}, and σ_p^{es} ($\xi_u = 2\%$, $T_u = 2.5$ s, $T_f = 5.0$ s, $\alpha_{sy} = 0.025$, $\delta_{sy} = 2.5$ cm, and Force 02 in the across-wind direction).

References

1. The Japan Society of Seismic Isolation. *MENSHIN, No. 117*; The Japan Society of Seismic Isolation: Tokyo, Japan, 2022. (In Japanese)
2. Li, J.; Luo, W.; Liang, Q.; Wang, D.; Zhou, Y.; He, Z. Shaking table test of seismic performance of high-rise over-track building with base isolation. *J. Build. Eng.* **2023**, *75*, 106749. [CrossRef]
3. Kitamura, H. *Seismic Responses Analysis Methods for Performance Based Design*, 2nd ed.; Shokokusha Publishing: Tokyo, Japan, 2009. (In Japanese)
4. Architectural Institute of Japan. *Design Recommendations for Seismically Isolated Buildings*; Architectural Institute of Japan: Tokyo, Japan, 2016.
5. Khatibinia, M.; Jalaipoura, M.; Gharehbaghi, S. Shape optimization of U-shaped steel dampers subjected to cyclic loading using an efficient hybrid approach. *Eng. Struct.* **2019**, *197*, 108874. [CrossRef]
6. Yu, T.; Zhang, C.; Huang, Z.; Huang, W.; Wang, S.; Zhong, G.; Ou, D. Experimental and numerical studies of a novel three-dimensional isolation device incorporating disc springs with U-shaped dampers. *Soil Dyn. Earthq. Eng.* **2023**, *174*, 108164. [CrossRef]
7. Pang, H.; Yang, Q.; Liu, M.; Hui, Y.; Cheng, B. The Influence of Wind Direction on the Inelastic Responses of a Base-Isolated Square Section High-Rise Building. *Buildings* **2022**, *12*, 1208. [CrossRef]
8. Tian, J.; Chen, X. 3D coupled wind-induced inelastic response of base-isolated tall buildings with eccentricity and biaxial interaction of hysteretic restoring base forces. *J. Wind Eng. Ind. Aerodyn.* **2023**, *232*, 105252. [CrossRef]
9. Li, Z.; Chen, X.; Huang, G.; Kareem, A.; Zhou, X. Alongwind and crosswind response of friction-pendulum base-isolated high-rise buildings. *Eng. Struct.* **2023**, *293*, 116564. [CrossRef]
10. Li, Z.; Huang, G.; Chen, X.; Zhou, Y.; Yang, Q. Wind-resistant design and equivalent static wind load of base-isolated tall building: A case study. *Eng. Struct.* **2020**, *212*, 110533. [CrossRef]
11. Qian, X.; Sato, D. Evaluation of residual deformation in seismic isolation layer based on typhoon simulation. *J. Struct. Eng.* **2020**, *66*, 323–329. (In Japanese)
12. Lu, Z.; Brennan, M.; Ding, H.; Chen, L. High-static-low-dynamic-stiffness vibration isolation enhanced by damping nonlinearity. *Sci. China Technol. Sci.* **2018**, *62*, 1103–1110. [CrossRef]
13. Qian, X.; Sato, D.; Mabashi, S. Effects of building aspect ratio on fatigue damage of steel dampers installed in base-isolated high-rise buildings. In Proceedings of the 15th International Conference on Wind Engineering, Beijing, China, 1–6 September 2019.
14. Kishiki, S.; Ohkawara, Y.; Yamada, S.; Wada, A. Experimental evaluation of cyclic deformation capacity of U-shaped steel dampers for base-isolated structures. *J. Struct. Constr. Eng.* **2008**, *73*, 333–340. (In Japanese) [CrossRef]
15. Jiao, Y.; Kishiki, S.; Yamada, S.; Ene, D.; Konishi, Y.; Hoashi, Y.; Terashima, M. Low cyclic fatigue and hysteretic behavior of U-shaped steel dampers for seismically isolated buildings under dynamic cyclic loadings. *Earthq. Eng. Struct. Dyn.* **2014**, *44*, 1523–1538. [CrossRef]
16. The Japan Society of Seismic Isolation. *Guidelines for the Wind-Resistant Design of Seismically Base-Isolated Buildings*; The Japan Society of Seismic Isolation: Tokyo, Japan, 2018.
17. Akiyama, H. *Earthquake-Resistant Design Method for Buildings Based on Energy Balance*; Gihodo Shuppan: Tokyo, Japan, 1999. (In Japanese)
18. Yoshie, K.; Kitamura, H.; Ohkuma, T. A study of wind-induced energy input to an elasto-plastic structure. *J. Struct. Constr. Eng.* **2003**, *68*, 31–38. (In Japanese) [CrossRef]
19. Yoshie, K.; Kitamura, H.; Ohkuma, T. A prediction method for response of an elasto-plastic structure to fluctuating wind force based on energy balance. *J. Struct. Constr. Eng.* **2005**, *70*, 59–66. (In Japanese) [CrossRef] [PubMed]
20. Yoshie, K.; Ohkuma, T.; Kitamura, H.; Wada, A. Probability distribution function of response amplitude for an elasto-plastic structure subjected to wide-band fluctuating wind force. *J. Struct. Constr. Eng.* **2006**, *71*, 37–46. (In Japanese) [CrossRef] [PubMed]

21. Yoshie, K.; Kitamura, H.; Ohkuma, T.; Wada, A. A prediction method for response of an elasto-plastic structure to wide-band fluctuating wind force with non-zero mean component based on energy balance. *J. Struct. Constr. Eng.* **2006**, *71*, 21–28. (In Japanese) [CrossRef] [PubMed]
22. Yoshie, K.; Kitamura, H.; Ohkuma, T. A study on fluctuating wind-force induced energy input to an elasto-plastic structure. In Proceedings of the 6th Asia-Pacific Conference on Wind Engineering, Seoul, Repubic of Korea, 12–14 September 2005.
23. Yoshie, K.; Kitamura, H.; Ohkuma, T. A prediction method for response of an elasto-plastic structure to fluctuating wind force based on energy balance. In Proceedings of the Council on Tall Buildings and Urban Habitat 7th World Congress, New York City, NY, USA, 16–19 October 2005.
24. Rigon, D.; Berto, F.; Meneghetti, G. Estimating the multiaxial fatigue behaviour of C45 steel specimens by using the energy dissipation. *Int. J. Fatigue* **2021**, *151*, 106381. [CrossRef]
25. Simiu, E.; Yeo, D. *Wind Effects on Structures: Modern Structural Design for Wind*; John Wiley & Sons: Hoboken, NJ, USA, 2019.
26. Meskouris, K.; Butenweg, C.; Hinzen, K.G.; Höffer, R. *Structural Dynamics with Applications in Earthquake and Wind Engineering*, 2nd ed.; Springer: Berlin, Germany, 2019.
27. Hutt, C.M.; Vahanvaty, T.; Kourehpaz, P. An analytical framework to assess earthquake-induced downtime and model recovery of buildings. *Earthq. Spectra* **2022**, *38*, 1283–1320. [CrossRef]
28. Forcellini, D. An expeditious framework for assessing the seismic resilience (SR) of structural configurations. *Structures* **2023**, *56*, 105015. [CrossRef]
29. Kasai, K.; Chimamphant, S.; Matsuda, K. Performance curves for base-isolated buildings reflecting effect of superstructure vibration period. *J. Struct. Constr. Eng.* **2016**, *81*, 239–249. (In Japanese) [CrossRef]
30. Architectural Institute of Japan. *AIJ Recommendations for Loads on Buildings (2015)*; Architectural Institute of Japan: Tokyo, Japan, 2015.
31. Sato, D.; Kasai, K.; Tamura, T. Influence of frequency sensitivity of viscoelastic damper on wind-induced response. *J. Struct. Constr. Eng.* **2009**, *74*, 75–82. (In Japanese) [CrossRef]
32. Omiya, M.; Kitamura, H. Investigation and analysis on the structural characteristics of the recent base isolated buildings corresponding to long-period ground motion. *AIJ J. Technol. Des.* **2019**, *25*, 61–66. (In Japanese) [CrossRef]
33. Roesset, J.M.; Whitman, R.V.; Dobry, R. Modal Analysis for Structures with Foundation Interaction. In Proceedings of the ASCE National Structural Engineering Meeting, Cleveland, OH, USA, 24–28 April 1972. Structures Publication No. 329.
34. Demir, A.; Kayhan, A.H.; Palanci, M. Response- and probability-based evaluation of spectrally matched ground motion selection strategies for bi-directional dynamic analysis of low- to mid-rise RC buildings. *Structures* **2023**, *58*, 105533. [CrossRef]
35. Charmpis, D.C.; Komodromos, P.; Phocas, M.C. Optimized earthquake response of multi-storey buildings with seismic isolation at various elevations. *Earthq. Eng. Struct. Dyn.* **2012**, *41*, 2289–2310. [CrossRef]
36. Forcellini, D.; Kalfas, K.N. Inter-story seismic isolation for high-rise buildings. *Eng. Struct.* **2023**, *275*, 115175. [CrossRef]
37. Hao, R.-B.; Lu, Z.-Q.; Ding, H.; Chen, L.-Q. Shock Isolation of an Orthogonal Six-DOFs Platform with High-Static-Low-Dynamic Stiffness. *J. Appl. Mech.* **2023**, *90*, 111004. [CrossRef]
38. Cui, W.; Zhao, L.; Ge, Y. Wind-Induced Buffeting Vibration of Long-Span Bridge Considering Geometric and Aerodynamic Nonlinearity Based on Reduced-Order Modeling. *J. Struct. Eng.* **2023**, *149*, 04023160. [CrossRef]